Tin dispersed in a calcium silicate matrix: A composite oxide as anode material for Li-ion batteries

M. Mouyane [1], M. Womes, J.C. Jumas, J. Olivier-Fourcade, P.E. Lippens *

Institut Charles Gerhardt (ICG), UMR 5253 CNRS, Equipe Agrégats, Interfaces et Matériaux pour l'Energie, Université Montpellier II, CC 1502, 34095 Montpellier Cedex 5, France

ABSTRACT

The electrochemical reaction mechanism of the $Sn-(CaSiO_3)_{0.4}$ composite electrode with Li was investigated by electrochemical tests and a variety of spectroscopic techniques. The electrochemical behavior of this material showed a highly reversible reaction with Li after the first discharge with a specific capacity of 530 mAh g^{-1} at C/10 rate. Some essential steps of the mechanism have been inferred from ^{119}Sn Mössbauer spectroscopy and the electrochemical potential curve. The composite material contains three tin based phases with different tin oxidation numbers: an amorphous Sn^{II} phase which is reduced into Sn^0 as the first step of the discharge, $CaSn^{IV}SiO_5$ and β-Sn which are progressively transformed into lithium–tin alloys during the discharge. A Mössbauer spectrum recorded at the end of the discharge reveals the formation of Li_7Sn_2. The de-alloying reaction of Li_7Sn_2 leads to the formation of β-Sn at the end of the charge. X-ray absorption and ^{119}Sn Mössbauer spectroscopy revealed furthermore that the electrochemical reaction between Li and the $Sn-(CaSiO_3)_{0.4}$ composite is accompanied by an electron transfer between Li and Sn.

© 2011 Elsevier B.V. All rights reserved.

1. Introduction

Due to their exceptional properties in terms of high specific energy, long cycle life and ambient temperature operation, rechargeable lithium-ion batteries have become an important source for powering many applications such as computers, telecommunication equipment, or electric and hybrid vehicles [1,2]. Graphite is used as anode for commercial lithium-ion batteries due to its flat charge and discharge plateaus and excellent cycling stability. However, the low theoretical capacity of the carbon material (372 mAh g^{-1}) limits its use for new applications. Sn-based materials have been suggested as promising alternative anodes as tin is able to form a number of intermetallic compounds with lithium. Electrochemical cycling between metallic tin and the lithium-richest of these compounds, $Li_{22}Sn_5$, corresponds to a storage capacity of 991 mAh g^{-1} [3]. Moreover, the tin electrode operates in the favorable voltage range of 0.25–0.5 V *vs.* Li metal. However, the large volume variations occurring during lithiation and de-lithiation constitute a serious problem of this material. They cause a structural instability of the electrode, resulting in

poor cyclic performance. Several strategies have been considered to minimize the effects of this problem, such as nano-sized tin [4], tin-metal alloys [5,6], tin oxide [7], tin composite oxides (TCO) [8,9] and, recently, metallic tin dispersed in a composite oxide [10,11]. The aim of the latter two strategies is to disperse the electrochemically active material in an inactive matrix which buffers the volume expansion, maintains in this way the dispersion of tin at a high level and guarantees good mechanical and electrical contacts between the particles. For example the use of composite materials such as $Sn-BPO_4$ and $Sn-CaSiO_3$ improved the reversible cycling behavior as compared with pure β-Sn [12–14].

In the present study, the concept of dispersing metallic tin in an inactive matrix is applied to the new composite material $Sn-CaSiO_3$. The performances of this material as a negative electrode in Li-ion batteries were analyzed. The formation of Li–Sn compounds during the lithiation and delithiation processes were studied by X-ray diffraction (XRD), ^{119}Sn Mössbauer spectroscopy and X-ray absorption spectroscopy (XAS).

Our paper is organized as follows. After some experimental details we first give a brief summary of a study of the starting material by XRD, scanning electron microscopy (SEM), energy dispersive X-ray analysis (EDX) and ^{119}Sn Mössbauer spectroscopy the details of which can be found elsewhere [15]. A structural model derived from these results will be presented. The next section will be devoted to the determination of the probabilities of recoilless absorption of gamma radiation for all phases observed by Mössbauer spectroscopy in the starting material. These data

* Corresponding author. Tel.: +33 4 67 14 45 48; fax: +33 4 67 14 33 41.
 E-mail address: lippens@univ-montp2.fr (P.E. Lippens).
[1] Present address: Laboratoire Universitaire des Sciences Appliquées de Cherbourg (LUSAC), EA 4253, Université de Caen Basse-Normandie, BP 78, 50130 Cherbourg Octeville, France.

will be then be used for a quantitative analysis of the electrochemical reaction of the composite material with lithium, based on a galvanostatic discharge curve and on results obtained from Mössbauer spectroscopy. An attempt will be made to attribute characteristic plateaus of the discharge curve to the formation of specific intermediate reaction products. The last section will demonstrate the influence of the current density applied during discharge and charge on the electrochemical reaction mechanism and on its reversibility.

2. Experimental

The composite material was prepared in two steps. First, the $CaSiO_3$ matrix was synthesized by a sol–gel method from a stoichiometric mixture of tetraethyl orthosilicate and calcium nitrate tetrahydrate. The calcium silicate gel was dried in an oven at 80 °C overnight and calcined at 730 °C for 4 h in order to remove nitrate and residual organic groups. The $Sn–(CaSiO_3)_{0.4}$ composite was synthesized in a second step by a solid-state reaction of the $CaSiO_3$ matrix with Sn (Aldrich, diameter <10 μm). These reagents were mixed, ground and fired in a vitreous carbon heating boat inside a horizontal tube furnace in argon atmosphere at 850 °C for 7 h, then allowed to cool down to room temperature by quenching, after removing the boat from the furnace. The solid formed in this way was carefully ground to a fine powder.

Electrochemical tests were carried out in Swagelok two-electrode cells under galvanostatic conditions at constant current densities in a potential window between 0.01 and 1.2 V *vs.* Li^+/Li^0. The tests were controlled by a MacPile II automated system. $Sn–(CaSiO_3)_{0.4}$ working electrodes were prepared as pellets by pressing a mixture of 80 wt.-% active material, 10 wt.-% polytetrafluoroethylene (PTFE) binder and 10 wt.-% carbon black to improve the mechanical and electric properties. A lithium foil was used as the negative electrode. The electrolyte consisted of 1 M $LiPF_6$ in 1:1:3 in vol. ratio mixture of propylene carbonate (PC)/ethyl carbonate (EC)/dimethyl carbonate (DMC), and Whatman paper (borosilicate glass microfiber filters) was used as separator. The cells were assembled in a glove box under dry argon atmosphere. The reaction mechanism in the $Sn–(CaSiO_3)_{0.4}$ electrode, was analyzed by ^{119}Sn Mössbauer spectroscopy, XRD and XAS at different depths of the electrochemical reaction. To this end the lithium insertion was stopped at various voltages. The cells were then opened inside the glove box and the electrodes were transferred to specific air-tight sample-holders equipped with radiation transparent windows.

The structural characterization of the samples was done by powder X-ray diffraction (XRD) on a Philips X'Pert diffractometer using Cu Kα radiation (λ = 1.5418 Å). ^{119}Sn Mössbauer spectra were recorded at room temperature in transmission geometry on a standard instrument operated in the constant acceleration mode. The γ-ray source of ^{119m}Sn in a $BaSnO_3$ matrix had a nominal activity of 370 MBq. The velocity scale was calibrated using the magnetic sextet of a high purity iron foil as a standard spectrum and a $^{57}Co(Rh)$ source. Isomer shifts are given with respect to $BaSnO_3$ at room temperature. The spectra were evaluated by fitting Lorentzian profiles to the experimental data using a least-squares method [16]. The fit quality was controlled by the classical χ^2 test. X-ray absorption experiments at the Sn L_I-edge were carried out at room temperature at the CCLRS laboratory (Daresbury, UK) using synchrotron radiation. The Sn L_I-edge was recorded in transmission geometry on beamline 7.1 which was equipped with a Si(1 1 1) monochromator. The beam intensities I_0 and I before and after the sample were measured with ion chambers filled with He/Ar. All spectra were corrected for a linear baseline which was fitted to the pre-edge part, and were normalized to give identical absorption steps between baseline and the energy domain of pure atomic absorption. The

energy scale was calibrated by setting the maximum of the first derivative of the L_I-edge spectrum of a Sn foil to 4465 eV.

3. Results

3.1. Characterization of the composite material

A previous study based on XRD, SEM and EDX has shown that the composite material is mainly composed of SiO_2, β-$CaSiO_3$, $CaSnSiO_5$, and particles of β-Sn with a diameter of approximately 10 μm. The halo observed in the X-ray diffractograms suggested, in addition to these crystalline species, the presence of an amorphous phase [15]. Further insight was gained from ^{119}Sn Mössbauer spectroscopy in both transmission and backscattering geometry. The spectra revealed the existence of three Sn oxidation states: Sn^0, Sn^{IV} and Sn^{II}. Comparison of the Mössbauer parameters with data reported in the literature allowed attributing them to β-Sn, $CaSnSiO_5$ and amorphous tin-silicates, respectively. A structural model was developed in [15] according to which the metallic tin particles are embedded in a matrix of SiO_2, β-$CaSiO_3$ and $CaSnSiO_5$, with amorphous Sn^{II}-silicates and Sn^{IV}-oxide forming the interface between tin particles and the matrix.

Based on this model, published values of the Lamb–Mössbauer factors f for similar tin based materials were used in [15] for a rough evaluation of the different amounts of tin phases in the composite. For a more quantitative evaluation, we have now experimentally determined the values of f for the three tin-based phases corresponding to the tin oxidation states observed in the composite by recording their Mössbauer spectra as a function of temperature between 76 and 293 K. Fig. 1 shows as examples the spectra obtained for the composite material $Sn–(CaSiO_3)_{0.4}$ at these two temperatures. The corresponding hyperfine parameters are given in Table 1.

In the case of thin absorbers, the temperature dependence of the Lamb–Mössbauer factor can be derived from the variations of the area A under the resonance curve of each tin oxidation state as a function of temperature [17]. By considering the Debye model in the high-temperature limit, one can write [18]

$$\frac{d \ln A}{dT} = \frac{d \ln f}{dT} = \frac{-6E_R}{K_B \theta_M^2} \tag{1}$$

where E_R is the recoil energy of the γ-ray (2.572×10^{-3} eV for ^{119}Sn), θ_M is the Debye temperature of the phase measured by
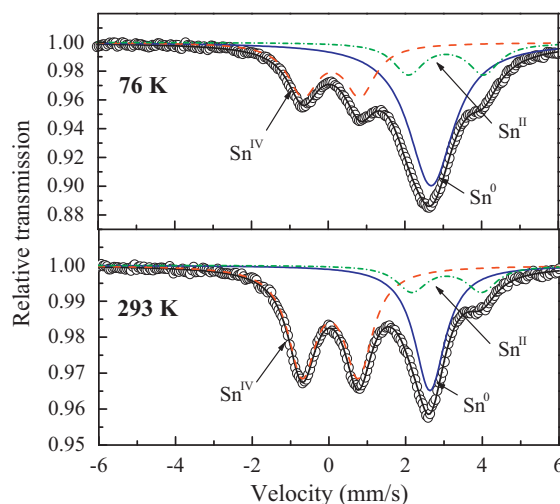

Fig. 1. ^{119}Sn Mössbauer spectra of the composite material $Sn–(CaSiO_3)_{0.4}$ at 76 and 293 K. The subspectra reflect the contributions of the three tin phases: Sn^0 (solid line), Sn^{II} (dash-dotted line) and Sn^{IV} (dashed line).

Table 1
Hyperfine parameters obtained from ^{119}Sn Mössbauer spectra shown in Fig. 1.

Temperature (K)	Tin phases	δ (mm s^{-1})	Δ (mm s^{-1})	2Γ (mm s^{-1})	Area
76	Sn^0	2.59 (1)	0.42 (2)	1.08 (4)	288.3 × 10^{-4}
	Sn^{II}	2.92 (1)	1.98 (2)	1.20 (3)	159.7 × 10^{-4}
	Sn^{IV}	−0.01 (1)	1.48 (1)	0.96 (1)	173.7 × 10^{-4}
293	Sn^0	2.54 (1)	0.28 (2)	0.81 (4)	763.6 × 10^{-5}
	Sn^{II}	2.93 (2)	1.85 (2)	1.04 (4)	408.2 × 10^{-5}
	Sn^{IV}	−0.06 (1)	1.46 (1)	0.90 (1)	131.1 × 10^{-4}

Isomer shift (δ) relative to BaSnO$_3$, quadrupole splitting (Δ), line width at half maximum (2Γ) and the area under the spectra (Area).
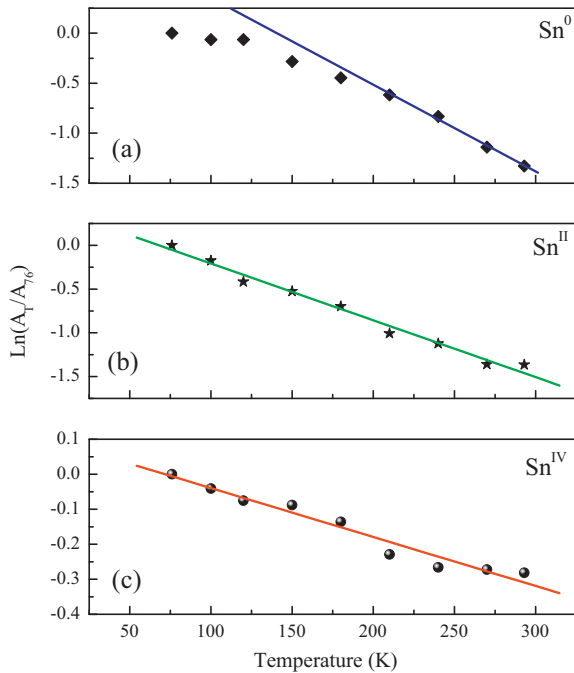

Fig. 2. Temperature dependence of the normalized areas under the resonance curves A_T/A_{76}, where A_{76} is the area at 76 K, for the three tin phases in Sn–(CaSiO$_3$)$_{0.4}$: Sn^0 (a), Sn^{II} (b) and Sn^{IV} (c).

Mössbauer spectroscopy, and K_B is the Boltzmann constant. Thus, in the high-temperature limit the experimental values of $\ln(A(T))$ are expected to be linearly correlated with the temperature with a slope (α) which gives the values of θ_M and f:

$$f(T) = \exp(\alpha T) \tag{2}$$

Our experimental data obtained for the different tin oxidation states of the composite show that $\ln(A_T/A_{76})$ decreases linearly in the high temperature range in good agreement with Eq. (1) (Fig. 2).

We have determined the slopes α from linear regression for all three tin species. The values of the slopes and f factors at 300 K are reported in Table 2. For Sn^{IV} our value 0.66 is close to that previously published for CaSnSiO$_5$ [19,20] in good agreement with our previous attribution of this sub-spectrum to malayaite based on the values of the isomer shift and quadrupole splitting. For Sn^0, the value of $f = 0.07$ is within the range of published values for β-Sn [21]. The Mössbauer isomer shift and quadrupole splitting

Table 2
Values of the slopes determined from linear regression of area logarithm. Experimental Lamb–Mössbauer factors are given at 300 K for the three Sn^0, Sn^{II}, Sn^{IV} based phases.

	Sn^0	Sn^{II}	Sn^{IV}
$\alpha = \frac{d}{dT} \ln\left(\frac{A_T}{A_{76}}\right)$ K^{-1}	−8.76 × 10^{-3}	−6.49 × 10^{-3}	−1.40 × 10^{-3}
f-Factor at 300 K	0.07	0.14	0.66

obtained for Sn^{II} are comparable with those of tin based silicates [22,23] but there is no reported Lamb–Mössbauer value for such material. However, the present value of 0.14 is similar to that of tin borophosphate glasses [21].

In the following, two discharge runs will be examined by Mössbauer spectroscopy, one at C/50 rate and one at C/10 rate. The respective starting materials, obtained from two separate syntheses, will be labeled *S50* and *S10*. Table 3 gives for all three tin species in the two composite materials Sn–(CaSiO$_3$)$_{0.4}$ the relative sub-spectrum areas derived from the fit and the relative amounts after correction for the different *f*-factors. The corrected relative amounts differ strongly from the relative sub-spectrum areas due to large differences between the values of *f* for the three phases, which justifies the present determination of *f* for the composite. The observed differences in sample composition of about 10% are mainly due to the synthesis conditions especially during the cooling process. The presence of SnO$_2$ (2%) in sample *S50* is probably accidental and we believe this phase to be an impurity of the starting material.

3.2. Electrochemical properties and phase analysis of the first discharge at C/50 rate

A typical voltage profile of the first discharge of a Sn–(CaSiO$_3$)$_{0.4}$ composite electrode recorded at C/50 rate between 1.2 and 0.01 V (*vs.* Li$^+$/Li^0) is shown in Fig. 3. During the initial discharge two shoulders can be observed at 1.5 and 0.80 V which are followed by three plateaus at about 0.68, 0.62 and 0.42 V, extending from 0.45 to 2.8 Li, before the voltage finally decreases gradually to 0.01 V. During the first discharge down to 0.01 V, a total amount of 4.45 Li per Sn–(CaSiO$_3$)$_{0.4}$ formula unit has reacted, which corresponds to a specific capacity of 720 mAh g^{-1}.

The theoretical values of the electrochemical potential of the successive alloying reactions of Li$_x$Sn compounds previously calculated from the linearized augmented plane wave (LAPW) method based on the density functional theory (DFT) are also reported in Fig. 3 [24]. The theoretical curve shows that the first Li$_x$Sn compounds are formed at potentials of 0.76 V (Li$_2$Sn$_5$) and 0.68 V (LiSn). Beyond 1 Li reacted, a large plateau is found at 0.48 V corresponding to the formation of Li$_7$Sn$_3$, which is followed at very close potentials of 0.49 V and 0.53 V by the formation of Li$_5$Sn$_2$ and Li$_{13}$Sn$_5$, respectively. These very similar potentials make the latter three compounds hardly distinguishable on an experimental voltage profile. This can be related to very close formation energies for these

Table 3
Relative area under the resonance curve (A%) and relative amounts corrected for *f*-factors (*RA*%) of the tin phases in the two samples, *S10* and *S50*, used for the study of the mechanisms at C/10 and C/50 regimes, respectively.

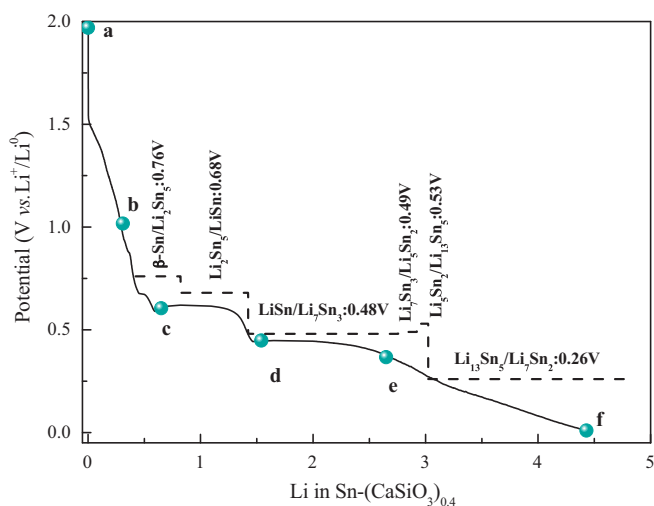| Samples		Sn^0	Sn^{II}	Sn^{IV}	SnO$_2$
S10	A (%)	55	15	30	–
	RA (%)	84	11	5	
S50	A (%)	42	22	25	11
	RA (%)	74	19	5	2

Fig. 3. First galvanostatic discharge curve of the Sn–(CaSiO$_3$)$_{0.4}$/Li half cell at C/50 rate. XRD and ^{119}Sn Mössbauer measurements were done at the points a, b, c and f. ^{119}Sn Mössbauer analysis was also carried out at point d. Comparison with theoretical electrochemical potentials of the formation of Li$_x$Sn intermetallic compounds calculated by the LAPW method.
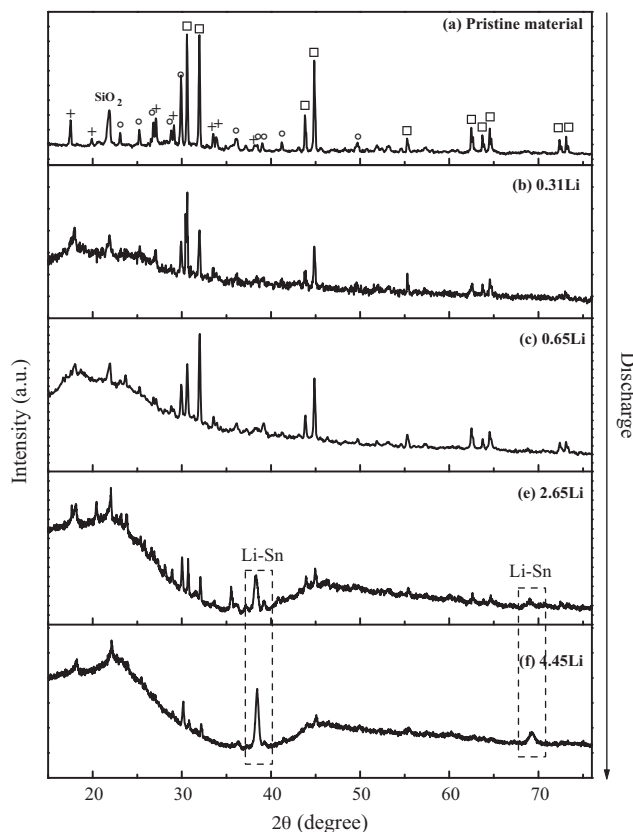

Fig. 4. XRD patterns for the points shown in Fig. 3: the pristine material (a), the electrode after the electrochemical reaction of 0.3 Li (b), of 0.65 Li (c), of 2.65 Li (e) and the electrode at the end of the first discharge (f). Open squares, open circles and crosses correspond to diffraction peaks of β-Sn, β-CaSiO$_3$ and CaSnSiO$_5$ respectively. The dashed rectangles show the domains for lithium–tin alloys. A peak of SiO$_2$ is also found.

three compounds, which is due to their close compositions and their similar structural organization based on a two-dimensional lattice characterized by alternating layers of lithium and tin atoms [25]. The last phase considered in the LAPW calculations, Li$_7$Sn$_2$, is formed at a potential of 0.26 V making it easily distinguishable from the latter three compounds.

Electrodes at different stages of the first discharge were analyzed by XRD and ^{119}Sn Mössbauer spectroscopy in order to investigate the role played by the amorphous tin-silicate (Sn^{II}) interface and to identify the exact composition of the Li$_x$Sn alloys formed during the first discharge. Their exact position on the discharge curve is indicated in Fig. 3. XRD patterns recorded at these points are shown in Fig. 4.

As described in Section 3.1, the XRD pattern of the starting material reveals the presence of the characteristic peaks of β-Sn, β-CaSiO$_3$, SiO$_2$, and CaSnSiO$_5$. The XRD patterns obtained for the lithiated electrode material in the first region of the discharge curve show a broad scattering band in the 15–30° range corresponding to the protective film. A peak at about 18° is due to PTFE. The main peaks of SiO$_2$ (21.85°) and β-CaSiO$_3$ (29.91°) can be observed on all the patterns of the first discharge. This indicates that both SiO$_2$ and β-CaSiO$_3$ of the composite do not react with Li. The peaks of β-Sn do not change noticeably until 0.65 Li and then strongly decrease. At the end of the discharge their amplitudes are very small but still observable, which indicates that a small amount of β-Sn did not react with Li during the discharge. The observed main peak of CaSnSiO$_5$ in the composite is at 17.51° just below the peak of PTFE. There are also two isolated peaks at about 34°. Their amplitudes are similar at the beginning of the discharge (samples b and c), then decrease at 2.65 Li (sample e) and are no longer observed at the end of discharge (sample f). This indicates that CaSnSiO$_5$ is transformed along the first discharge process. Finally, a new peak occurs at about 39° that can be attributed to Li–Sn phases [26]. The rather high intensity of this peak at the end of the first discharge as compared to the other peaks suggests that both β-Sn and CaSnSiO$_5$ were transformed into Li–Sn phases. However, the exact composition of these phases cannot be evaluated by only considering this XRD peak.

^{119}Sn Mössbauer spectroscopy was used to further elucidate the mechanism of the electrochemical reaction. The spectra are shown

in Fig. 5 and the hyperfine parameters of all observed phases are reported in Table 4.

In order to determine more precisely the composition of the Li–Sn alloys formed during the discharge, the experimental values of the isomer shift δ of the various discharge steps were reported on a reference diagram (Fig. 6). This diagram was obtained from the isomer shift mean value ($\bar{\delta}$) of the different Li–Sn crystalline phases (Li$_2$Sn$_5$, LiSn, Li$_7$Sn$_3$, Li$_5$Sn$_2$, Li$_{13}$Sn$_5$, Li$_7$Sn$_2$ and Li$_{22}$Sn$_5$) as a function of x, the Li/Sn ratio [25].

It can be seen from Fig. 6 that the isomer shift of the Li$_x$Sn crystalline phases decreases in a characteristic way with increasing Li/Sn ratio and % in Li. Two regions can be distinguished in Fig. 6: the first one comprises tin-rich alloys with a network based on Sn—Sn bonds that provides a strong covalo-metallic character. In these alloys, two atomic arrangements are present, a first one in which the Sn atoms are surrounded by six Sn and four Li atoms and a second one in which the Sn atoms are surrounded by four Sn and eight Li atoms. The second region comprises the lithium-rich alloys with Li-based lattices and some isolated molecule-like or atom-like Sn species. The samples analyzed at rates of C/50 and C/10 are marked by green solid stars and blue solid circles, respectively. The electrochemical mechanism at C/10 rate will be discussed in detail in Section 3.4.

The comparison between spectra (a) and (b) in Fig. 5 shows that the contribution of Sn^{II} atoms decreases. This confirms that the short plateau or shoulder at 1.5 V is mainly due to the reduction of the Sn^{II} amorphous phase. The short plateau at 0.86 V is related to the formation of a passivation film (solid electrolyte interphase, SEI) associated with the irreversible reduction of the electrolyte on
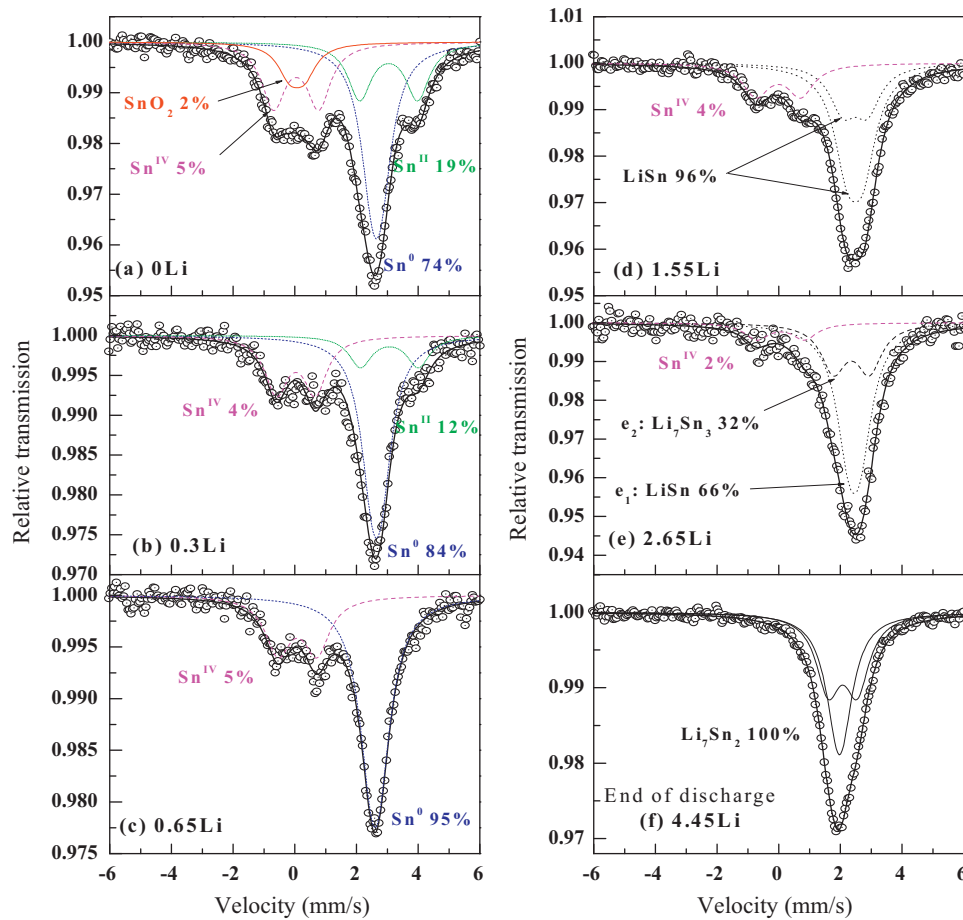
Fig. 5. ^{119}Sn Mössbauer spectra at room temperature for the points shown in Fig. 3.

the surface of the carbon particles [27]. In this region, we note that SnO_2 has completely disappeared (Fig. 5(b)) indicating the electrochemical reduction of the oxide at the same potential.

According to Mössbauer spectroscopy, the Sn^{II} amorphous phase was not detected in sample (c) (Fig. 5(c)) which is composed

by β-Sn (95%) and $CaSnSiO_5$ (5%) (Table 4). The absorption peak observed at point (d) (Fig. 5(d)), with an isomer shift of about $2.4\,mm\,s^{-1}$, is located in the region corresponding to tin-rich Li_xSn alloys (Fig. 6). The Mössbauer parameters are close to those of LiSn, which means that the first marked plateau at 0.62 V corresponds

Table 4
Hyperfine parameters obtained from the ^{119}Sn Mössbauer spectra shown in Fig. 5.

Sample	Tin phases	δ (mm s^{-1})	Δ (mm s^{-1})	2Γ (mm s^{-1})	A (%)	RA (%)	Abs.	χ^2
(a), 0Li	Sn^0	2.56[a]	0.29[a]	0.92[b]	42	74		
	Sn^{II}	2.95 (1)	1.88[a]	0.92[b]	22	19	5	0.53
	Sn^{IV}	−0.05 (3)	1.46 (3)	0.92[b]	25	5		
	Sn^{IV}O$_2$	−0.02 (3)	0.48[a]	0.92[b]	11	2		
(b), 0.3Li	Sn^0	2.56[a]	0.29[a]	0.89[b]	56	84		
	Sn^{II}	2.98[a]	1.88[a]	0.89[b]	16	12	3	0.67
	Sn^{IV}	−0.05[a]	1.26 (4)	0.89[b]	28	4		
(c), 0.65Li	Sn^0	2.52 (3)	0.23 (6)	1.00[b]	69	95	2	0.47
	Sn^{IV}	−0.01 (3)	1.26 (3)	1.00[b]	31	5		
(d), 1.55Li	Sn^{IV}	−0.05[a]	1.44[a]	1.02[b]	20	4		
	Sn$_1$(LiSn)	2.39 (1)	0.51 (2)	1.02[b]	53	63	5	0.57
	Sn$_2$(LiSn)	2.40 (2)	0.79 (1)	1.02[b]	27	33		
(e), 2.65Li	Sn^{IV}	−0.05[a]	1.45[a]	0.97[b]	10	2		
	e_1: Sn$_1$(LiSn)	2.36 (1)	0.38 (1)	0.97[b]	61	66	6	0.48
	e_2: Sn$_2$(Li$_7$Sn$_3$)	2.25 (6)	1.19 (9)	0.97[b]	29	32		
(f), 4.45Li	Sn$_1$(Li$_7$Sn$_2$)	1.99 (1)	0.94 (3)	0.94[b]	50	50	3	0.49
	Sn$_2$(Li$_7$Sn$_2$)	1.88 (3)	0.13 (5)	0.94[b]	50	50		

Isomer shift (δ) relative to BaSnO$_3$, quadrupole splitting (Δ), line width at half maximum (2Γ), relative area under the resonance curve (A%), relative amounts corrected for f-factors (RA%), absorption (Abs.) and goodness-of-fit (χ^2).

[a] Values imposed.
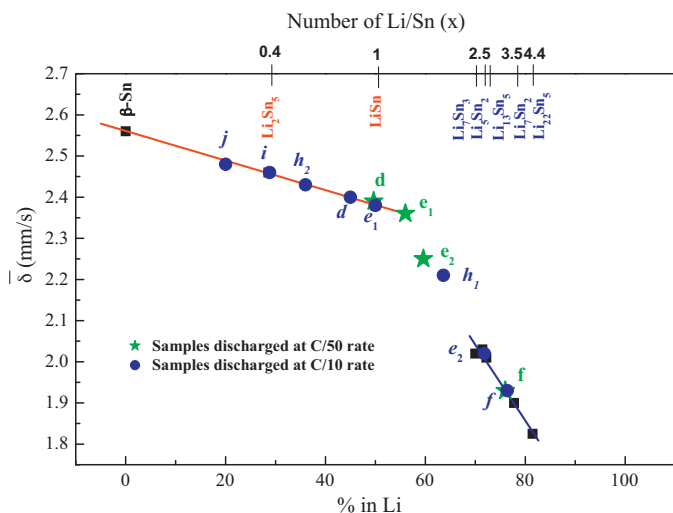[b] Values constrained to be equal.

Fig. 6. $\bar{\delta}$-%Li correlation diagram for Li–Sn alloys (black solid squares) and for the products obtained from lithiation of Sn–$(CaSiO_3)_{0.4}$ composite material at a rate of C/50 (green solid stars) and at a rate of C/10 (blue solid circles). (For interpretation of the references to color in this figure legend, the reader is referred to the web version of the article.)

to the transformation of β-Sn into LiSn. The contribution of the malayaite remains essentially unchanged (4%).

At point (e) (Fig. 5(e)) we observe two absorption peaks in the spectrum, labeled e_1 and e_2 (Table 4). The isomer shift of (e_1) corresponds to tin-rich alloys, while that of (e_2) is situated on the extension of the lithium-rich zone towards lower Li concentrations (Fig. 6). The peak (e_2) does not correspond to a well-defined Li_xSn composition. This can be explained by the coexistence of the three next lithium-rich alloys after LiSn: Li_7Sn_3, Li_5Sn_2, $Li_{13}Sn_5$ with close compositions and close isomer shift values. The observed main trend along the plateau (d and e) at 0.44 V is the decrease of the isomer shift which indicates the formation of lithium-rich alloys with compositions close to Li_7Sn_3. The amount of malayaite is very small (2%) but still detectable by Mössbauer spectroscopy because of the high value of the *f*-factor for this compound.

At the end of the first discharge, at point (f), all Sn^{IV} in malayaite has been reduced, a process which starts at point (d), and we observe the formation of 100% of an alloy richer in lithium than (e_1) and (e_2), with a composition close to Li_7Sn_2 (Fig. 5(f)).

The results reveal that the restructuring process during the first discharge corresponds to the reduction of certain tin oxides (amorphous Sn^{II} and SnO_2), to which is added the formation of a SEI, followed by an alloying process with the progressive formation of increasingly lithium-rich Li_xSn alloys leading to Li_7Sn_2 at the end of discharge.

The observed differences between the Li–Sn phases expected from the theoretical potential plateaus and the Mössbauer data, particularly for reactions with 2–3 Li can be explained by the presence of calcium since the malayaite is reduced at a potential of about 0.44 V leading to the formation of a mixed Li_xCa_ySn alloy and/or $CaSn_x + Li_xSn$ phases [19,28]. The hyperfine parameters of such a mixed alloy could deviate from those of pure Li–Sn phases.
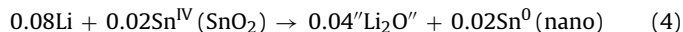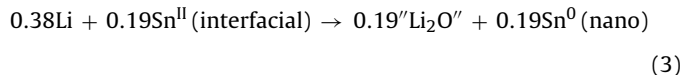
3.3. Quantitative analysis and reaction mechanism of the C/50 discharge

All these results allow suggesting the following electrochemical reaction mechanism for Li in the composite:

The first steps of the discharge, between points (a) and (c), which spread over 0.65 Li, represent the amount of lithium necessary to

reduce the amorphous interfacial Sn^{II} and SnO_2 and to form a SEI [27].

Based on the results obtained by Mössbauer spectroscopy (Table 4), the reactions can be written as follows:

$$0.38Li + 0.19Sn^{II}(\text{interfacial}) \rightarrow 0.19''Li_2O'' + 0.19Sn^0(\text{nano}) \tag{3}$$

$$0.08Li + 0.02Sn^{IV}(SnO_2) \rightarrow 0.04''Li_2O'' + 0.02Sn^0(\text{nano}) \tag{4}$$

The electrochemical reaction mechanism of Li with $CaSnSiO_5$ can be described by the following equation:

$$0.4Li + 0.05CaSnSiO_5$$
$$\rightarrow 0.15''Li_2O'' + 0.05''Li_xCaSn'' + 0.05SiO_2 \quad (x \approx 2) \tag{5}$$
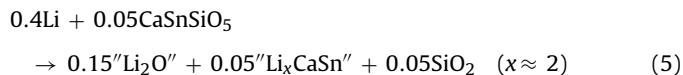
This reaction indicates that an electrochemical mechanism of $CaSnSiO_5$ is neither based on reversible insertion/extraction of lithium into host structures nor on solid solution but on conversion reaction leading to Li_xCaSn which denotes, for simplicity, a new ternary phase and/or Li_xSn and $CaSn_x$ phases [19]. One possible reason to justify such a proposal is the Mössbauer spectroscopy data which show that the electrochemical reaction of Li with $CaSnSiO_5$ occurs at 0.44 V in a potential of Li–Sn alloys formation.

Taking into account the proportion of β-Sn in the starting material (74%) and those obtained from the reduction of interfacial tin (II) (19%) and tin (IV) (SnO_2, $CaSnSiO_5$, 7%), the amount of active β-Sn is 100%. The reaction corresponding to the formation of the Li_7Sn_2 alloy (phase formed at the end of the discharge) is as follows:

$$7Li + 2\beta Sn \rightarrow Li_7Sn_2 \tag{6}$$

Thus, according to Eqs. (3)–(6), the amount of lithium deficit during the first discharge is almost negligible: $4.45 - (0.38 + 0.08 + 0.4 + 3.5) = 0.09$ Li and can be attributed to the formation of the SEI or reactions with the carbon used in the preparation of the electrode.

3.4. Influence of the discharge rate

We have focused our study on the first discharge which has been recorded over the potential range between 1.2 and 0.01 V at various rates: C/50, C/30, C/10, C/2 and C (Fig. 7).

For rates lower than C/30, the profiles are similar to that of C/30 while for rates higher than C/10 the profiles do not show a
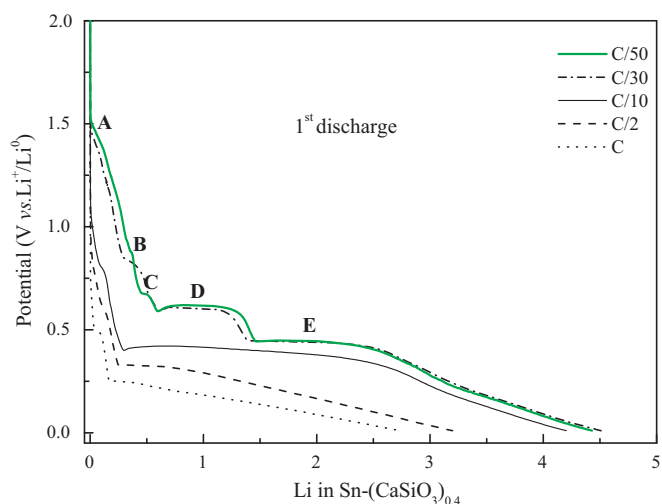

Fig. 7. First galvanostatic discharge for Sn–$(CaSiO_3)_{0.4}$ composite material tested in the range 1.2–0.01 V vs. Li^+/Li^0 obtained in galvanostatic mode at rate of C/50 (thick line), C/30 (dot dashed line), C/10 (thin line), C/2 (dashed line) and C (dotted line).
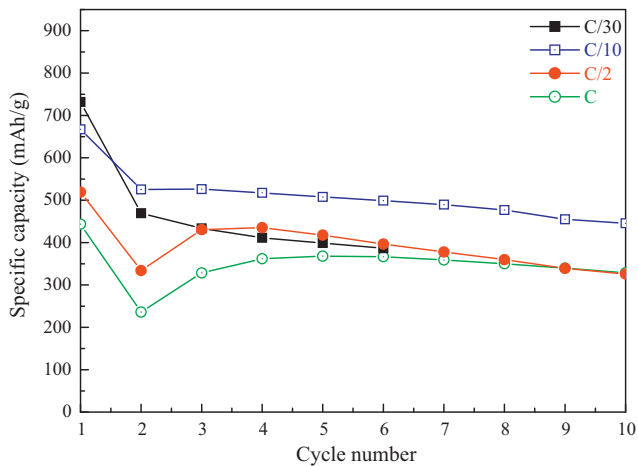
Fig. 8. Cycle life of the Sn–$(CaSiO_3)_{0.4}$ composite at a rate of C/30 (black solid squares), C/10 (blue open squares), C/2 (red solid circles) and C (green open circles). (For interpretation of the references to color in this figure legend, the reader is referred to the web version of the article.)

Fig. 9. First galvanostatic discharge curve of the Sn–$(CaSiO_3)_{0.4}$/Li half cell at C/10 rate. [119]Sn Mössbauer measurements were done at the points *a, c, d, e, f, h, i* and *j*. XAS measurements at points *b, c, e, f, g, h* and *j*.

well-defined plateau like that of C/10 but a continuously decreasing potential. For low discharge rates, the comparison of the potential profiles with the calculations suggests that plateaus labeled C ($\approx$0.7 V), D ($\approx$0.6 V) and E ($\approx$0.45 V) could be due to the formation of Li_2Sn_5, LiSn and a mixture of $Li_7Sn_3/Li_5Sn_2/Li_{13}Sn_5$, respectively. In the latter case, both the compositions and the energies of formation of the three phases are very close and they cannot be distinguished. As previously observed for Sn-based materials at very low rates the composition Li_7Sn_2 is expected to be formed during the decrease of the potential below about 0.4 V. The short plateau or shoulder A at about 1.5 V is only observed for slow discharges (C/50 and C/30). This is followed by a decreasing potential until 0.9 V which is similar to the potential profile observed for the transformation of the Sn^{II} amorphous phase to a Sn^0 based phase [13,29,30]. The short plateau B is related to the formation of a passivation film (solid electrolyte interphase, SEI) associated with the irreversible reduction of the electrolyte [27].

The potential profiles of the first discharge at higher Li rates do not show specific plateaus except for a shoulder at the beginning of the discharge (<0.1 Li). The potential of this shoulder decreases with increasing Li rate, which could be attributed to Li insertion into carbon or the formation of a SEI [27]. Then, the potential curve is formed by a plateau at C/10 or by a linearly decreasing potential for higher Li rates as expected from kinetic effects. There is also a clear tendency for the decrease of the maximum number of lithium (end of the discharge) with increasing Li rate, which leads to a decrease of the capacity.

The plateaus C–E were also observed during the charge/discharge cycles following the first discharge but with a polarization effect. Even for higher Li rates such as C/10 some plateaus were observed, which indicates differences in the electrochemical reactions from the first discharge. The total discharge capacities are of about 730 and 670 mAh g^{-1} at C/30 and C/10, respectively. However, large irreversible capacities were observed during the first discharge reducing the reversible capacity to about 460 and 530 mAh g^{-1} at C/30 and C/10, respectively.

Fig. 8 shows the specific capacity *vs.* discharge cycle number of the composite. The specific capacity of the first discharge decreases from 730 to 440 mAh g^{-1} as the Li rate increases from C/30 to C. In addition, the capacity strongly decreases at the second cycle by more than about 200 mAh g^{-1} for all Li rates. Then, we observe a stabilization or a slow decrease at low Li rate. At high Li rate the capacity first increases and then slowly decreases as in the case of C/30. Except for C/10 the capacity retention at the 10th cycle is
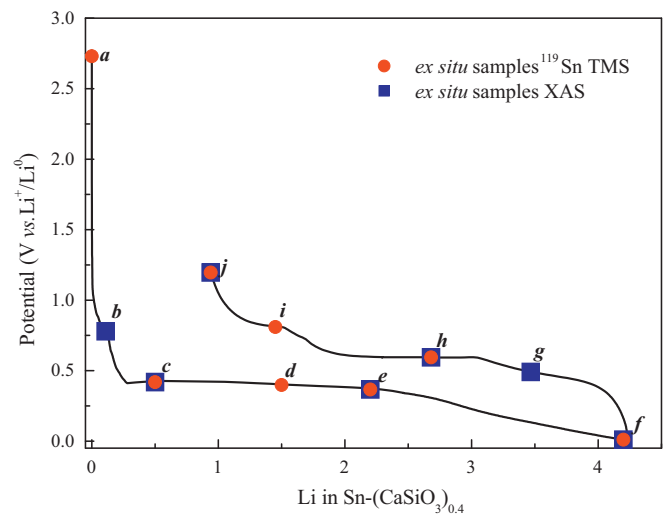
of about 70%, which seems to be the optimum for our experimental conditions (electrode formulation, cell design, *etc.*). However, in all cases the potential profiles obtained after the first discharge are very similar and the loss of capacity should be related to the texture of the electrode after the first discharge. Thus, the first discharge appears as an important step in the reorganization of the composite, leading to the dispersion of the active species in the restructured matrix, which has a strong impact on the electrochemical performances, the capacity loss during the first-cycle, the reversible capacity and the cycling life. At high rates, the restructuring is partial at the end of the first discharge and is complete after a few cycles. This explains the increase of the capacity at the second cycle. At slow rates, the restructuring is established at the end of the first discharge and leads to a different electrochemical behavior.

3.5. Discharge–charge mechanism at C/10 rate

As noticed before, the potential curve of the composite at C/10 differs from that at C/50 with the absence of distinct plateaus during the first discharge. Fig. 9 shows the first galvanostatic discharge–charge curve of the Sn–$(CaSiO_3)_{0.4}$ at C/10 rate.

The points analyzed by *ex situ* [119]Sn Mössbauer spectroscopy and by XAS at the Sn L_I-edge are indicated. The Mössbauer spectra of pristine and lithiated samples are shown in Fig. 10.

The Mössbauer parameters obtained from the experimental data and the relative amounts of the various tin species evaluated by considering the values of the Lamb Mössbauer factors are reported in Table 5.

The spectrum obtained after 0.5 Li (Fig. 10(c)) was fitted with two components that can be attributed to β-Sn (96%) and $CaSnSiO_5$ (4%). This indicates that Sn^{II} is reduced to Sn^0. Since the pristine material contained about 11% Sn^{II}, this reduction concerns 0.22 Li in agreement with the potential drop between 1 V and 0.7 V *vs.* Li^+/Li^0 at the beginning of the first discharge. By considering the short plateau or shoulder at about 0.7 V *vs.* Li^+/Li^0, the remaining 0.28 Li are involved in the formation of the a passivating film (SEI), by reduction reactions of Li with the electrolyte. Thus, we can consider that the first 0.5 Li were irreversibly used to transform the Sn^{II}-based interface and to form a SEI.

The spectrum obtained at 1.5 Li (Fig. 10(d)) shows a decrease of the $CaSnSiO_5$ doublet contribution and a broadening of the main Sn^0 peak. The latter peak was fitted with two doublets which give Mössbauer parameters close to those of LiSn [25]. The potential
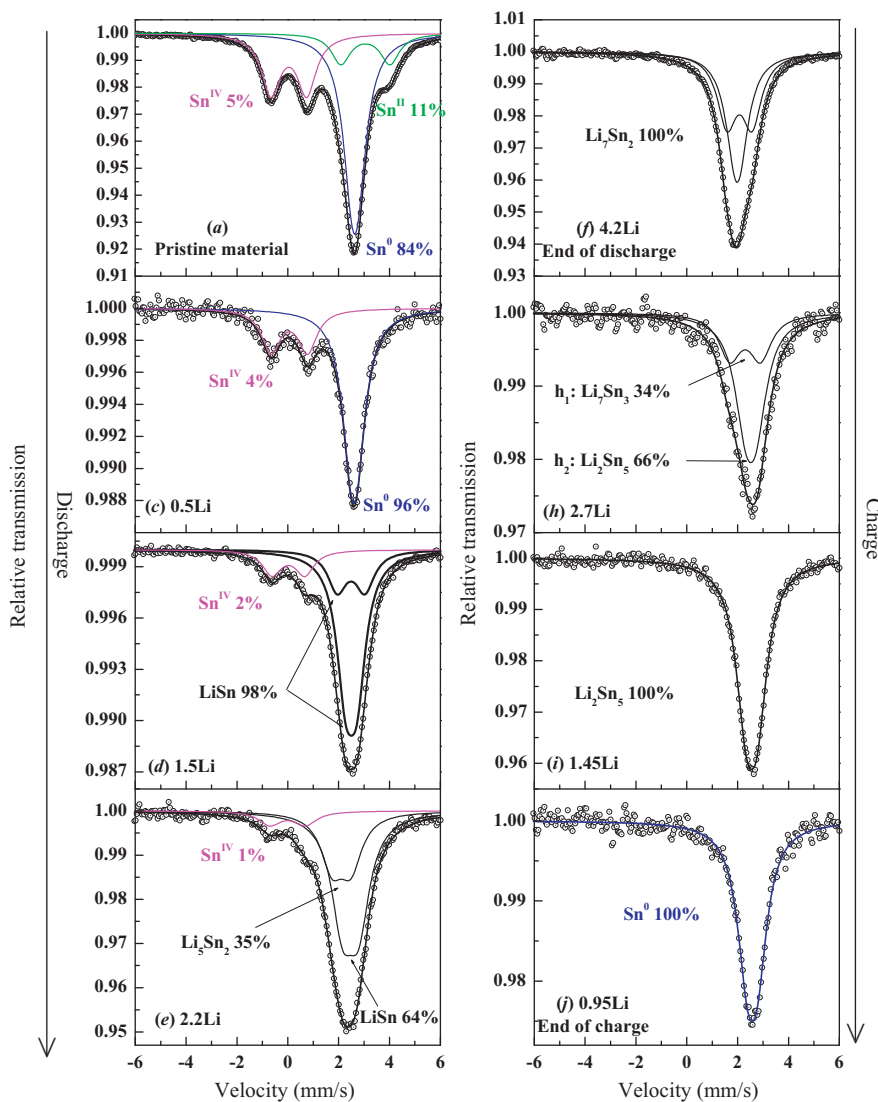
Fig. 10. ^{119}Sn Mössbauer spectra at room temperature for the points shown in Fig. 9.

value of the plateau, which is close to that of the plateau marked by the point (d) observed at C/50, is in good agreement with the calculated value for the LiSn alloy [24].

The main change observed in the spectrum of the sample (*e*) at the end of the plateau (2.2 Li) is the broadening and the velocity shift of the Sn^0 peak (Fig. 10(e)). For simplicity, we have just considered two doublets to fit this peak. The average value of the isomer shift (2.24 mm s^{-1}) is lower than that of the sample (*d*) suggesting more lithiated Li–Sn products. This value gives a composition of about 2Li/Sn (based on Fig. 6) in good agreement with the number of about 1.7 Li consumed on the plateau (Fig. 9). The values of the Mössbauer parameters for sample *f* (4.2 Li) (Fig. 10(f)) are close to those of crystalline Li_7Sn_2 except for the values of the quadrupole splitting which are slightly smaller, as previously observed for electrochemically formed Li_7Sn_2 [5]. This is due to the nanosize and/or the poor crystallinity of the products. The absence of Sn^{IV} contributions for this sample clearly indicates that $CaSnSiO_5$ is transformed at the potential of 0.4 V vs. Li$^+$/Li^0. This transformation is expected to use less than 0.4 Li based on the initial amount of $CaSnSiO_5$ evaluated from Mössbauer spectroscopy (5%), among which less than 0.2 Li are involved in the Sn^{II}/Sn^0 transformation. The number of Li used in the formation of this compound (sample *f*) is about 3.5 (Fig. 10(f)) in good agreement with the number of Li consumed at

the end of the discharge of about 4.2 Li (Fig. 9), taking into account the number of lithium used in reducing Sn^{II} and Sn^{IV} into Sn^0 and to form a SEI.

On charge, (h_1), the first of two species found at point (*h*) (Fig. 10(h)), is on the extension of the lithium-rich zone (Fig. 6) and its position is shifted towards lower isomer shifts as compared to the first tin-rich alloy (LiSn). The second species (h_2), as well as the phases found at points (*i*) and (*j*), are located in the region of isomers shift between 2.43 and 2.48 mm s^{-1} corresponding to tin-rich alloys (Fig. 6). The point (*i*) corresponds to Li_2Sn_5 (Fig. 10(i)). The position of (*j*) is located between Li_2Sn_5 and β-Sn, suggesting that the end of charge corresponds to the formation of a modified tin (Fig. 10(j)). Indeed, this Sn^0 is not exactly β-Sn due to the presence of some lithium particles remaining in the atomic network of tin.

The expected reaction from Li_7Sn_2 (end of discharge) to Li_2Sn_5 can be written as:

$$Li_7Sn_2 \rightarrow Li_2Sn_5 + 2.75Li \tag{7}$$

The reaction is not at equilibrium and still implies a slight deficit of lithium during the charge process of $3.5 - 2.75 - 0.4 = 0.35$ Li which can be explained by trapping of some of the lithium atoms

Table 5
Hyperfine parameters obtained from the [119]Sn Mössbauer spectra shown in Fig. 10.

Sample	Tin phases	δ (mm s^{-1})	Δ (mm s^{-1})	2Γ (mm s^{-1})	A (%)	RA (%)	Abs.	χ^2
(a), 0Li	Sn^0	2.54 (3)	0.22 (4)	0.90 (1)[b]	55	84	8	0.97
	Sn^{II}	2.96 (4)	1.93 (4)	0.90 (1)[b]	15	11		
	Sn^{IV}	−0.05 (3)	1.41 (4)	0.90 (1)[b]	30	5		
(c), 0.5Li	Sn^0	2.51 (3)	0.21 (8)	0.89 (1)[b]	71	96	1	0.43
	Sn^{IV}	−0.03 (3)	1.44 (6)	0.89 (1)[b]	29	4		
(d), 1.5Li	Sn$_1$(LiSn)	2.40 (1)	0.44 (1)	0.86 (4)	64	73	1	0.38
	Sn$_2$(LiSn)	2.39 (3)	1.09 (5)	0.89 (4)	22	25		
	Sn^{IV}	−0.08 (2)	1.29 (0)	0.89 (1)	14	2		
(e), 2.2Li	e_1: Sn$_1$(LiSn)	2.38 (1)	0.64 (1)	1.05 (2)	60	64	5	0.52
	e_2:Sn$_1$(Li$_5$Sn$_2$)	2.02 (3)	0.74 (2)	1.05 (4)	32	35		
	Sn^{IV}	−0.09 (6)	1.39 (7)	1.05 (1)	8	1		
(f), 4.2Li	Sn$_1$(Li$_7$Sn$_2$)	1.89 (1)	0.18 (1)	0.92 (1)[b]	50	50	6	0.5
	Sn$_2$(Li$_7$Sn$_2$)	1.98 (1)	0.98 (1)	0.92 (1)[b]	50	50		
(h), 2.7Li	h_1: Sn$_1$(Li$_7$Sn$_3$)	2.21 (3)	1.20 (6)	1.04 (4)[b]	34	34	3	0.57
	h_2: Sn$_1$(Li$_2$Sn$_5$)	2.43 (2)	0.42 (4)	1.04 (1)[b]	66	66		
(i), 1.45Li	Li$_2$Sn$_5$	2.46 (1)	0.45 (1)	0.97 (2)	100	100	4	0.4
(j), 0.95Li	Sn^0	2.48 (4)	0.29[a]	1.05 (5)	100	100	3	0.5

Isomer shift (δ) relative to BaSnO$_3$, quadrupole splitting (Δ), line width at half maximum (2Γ), relative area under the resonance curve (A%), relative amounts corrected for f-factors (RA%), absorption (Abs.) and goodness-of-fit (χ^2).

  [a] Value imposed.
  [b] Values constrained to be equal.

in the tin particles, in the matrix or at interfaces. The total electro-chemical reaction mechanism could be written as follow:

$$3.5Li + Sn^0 \rightarrow Li_7Sn_2 \qquad (8)$$

The first discharge/charge cycle at C/10 rate was also analyzed by *ex situ* X-ray absorption spectroscopy at the Sn L$_I$-edge. A spectrum of β-Sn is included for comparison. Fig. 11 shows that the X-ray absorption near edge structure (XANES) of β-Sn at the Sn L$_I$-edge exhibits a white line which is assigned to the electronic transition from the Sn 2s core level to the Sn 5p empty states at the bottom of the conduction band. The occurrence of a white line can be understood from the formal [Kr]$4d^{10}5s^25p^2$ electronic configuration of tin which gives rise to a partly filled 5p band.

The spectrum of sample (b), obtained after reaction with 0.1 Li, shows equally a white line, as expected from the presence of over 80% of tin in metallic form. Contributions from Sn^{II}- and Sn^{IV}-oxides, still present at this stage of the discharge process, contribute

to the L$_I$-edge absorption spectrum by their formal $5p^0$ electron configuration and might be responsible for the shoulder seen on the high energy side of the white line. During the further discharge, a progressively decreasing intensity of the white line with increasing lithium uptake is observed, indicating a reduction in the number of empty Sn 5p states. This observation proves the electron transfer from Li to Sn during the alloying process, which progressively fills the empty 5p states as the alloys become richer in lithium. During the charge the reversibility of the reaction is demonstrated by a progressive increase of the white line intensity suggesting the removal of electrons from the Sn 5p band during the dealloying process. This trend can be correlated with the variations of the Mössbauer isomer shift. The value of the [119]Sn Mössbauer isomer shift decreases with decreasing Sn 5s electron population and increasing Sn 5p electron population although the effect of the former electrons are about 10 times higher than that of the latter ones [31]. In the present case, the increase (decrease) of Sn 5p electron population suggested by
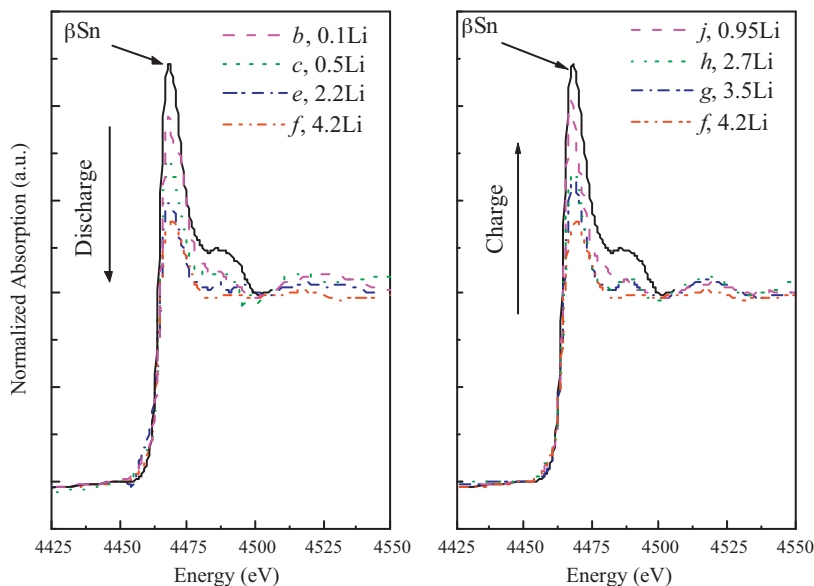

Fig. 11. Normalized XANES at the Sn L$_I$ X-ray absorption edge at room temperature for the points shown in Fig. 9.

XAS during the discharge (charge) is consistent with the observed decrease (increase) of the isomer shift for the Li_xSn phases reported in Table 5.

4. Conclusion

The electrochemical reaction mechanisms of $Sn–(CaSiO_3)_{0.4}$ composite as negative electrode for Li-ion batteries have been analyzed by XRD, ^{119}Sn Mössbauer spectroscopy and XAS. At both C/10 and C/50 rates, the tin based phases are transformed into Li_7Sn_2 at the end of the first discharge. Then, reversible de-alloying/alloying reactions take place between Li_7Sn_2 and poorly lithiated Sn(0) particles for the following charge/discharge cycles. Both the first discharge and the reversible reactions involve the formation of intermediate Li_xSn phases. The relative amounts of these Li_xSn phases were evaluated from ^{119}Sn Mössbauer spectroscopy as a function of the number of reacted lithium atoms. To this end, the Lamb–Mössbauer factors of all relevant phases were determined.

Compared to βSn based electrodes, the rather stable behavior of the composite, even at rates higher than C/10, shows that electrochemically inactive particles buffer the volume variations of the Li–Sn alloying reactions. This suggests that this material, due to its high energy density and high rate capability, could be used as anode material for Li-ion batteries.

Acknowledgements

References

[1] K. Tamura, T. Horiba, J. Power Sources 81 (1999) 156–161.
[2] K. Kohno, Y. Koishikawa, Y. Yagi, T. Horiba, J. Power Sources 185 (2008) 554–558.
[3] A.H. Whitehead, J.M. Elliott, J.R. Owen, J. Power Sources 82 (1999) 33–38.
[4] F. Wang, M.S. Zhao, X.P. Song, J. Power Sources 175 (2008) 558–563.
[5] S. Naille, M. Mouyane, M. El Amraoui, P.E. Lippens, J.C. Jumas, J. Olivier-Fourcade, Hyperfine Interact. 187 (2008) 19–26.
[6] L.Y. Beaulieu, D. Larcher, R.A. Dunlap, J.R. Dahn, J. Electrochem. Soc. 147 (2000) 3206–3212.
[7] J. Chouvin, J. Olivier-Fourcade, J.C. Jumas, B. Simon, P.H. Biensan, F.J.F. Madrigal, J.L. Tirado, C.P. Vicente, J. Electroanal. Chem. 494 (2000) 136–146.
[8] Y. Idota, T. Kubota, A. Matsufuji, Y. Maekawa, T. Miyasaka, Science 276 (1997) 1395–1397.
[9] Y. Idota, M. Mishima, Y. Miyaki, T. Kubota, J. Miyasaka, Patent No. 5618640 (1997).
[10] J.-H. Ahn, G.X. Wang, J. Yao, H.K. Liu, S.X. Dou, J. Power Sources 119–121 (2003) 45–49.
[11] Y. Zheng, J. Yang, Y.N. Nuli, J.L. Wang, J. Power Sources 174 (2007) 624–627.
[12] A. Aboulaich, M. Mouyane, F. Robert, P.E. Lippens, J. Olivier-Fourcade, P. Willmann, J.C. Jumas, J. Power Sources 174 (2007) 1224–1228.
[13] M. Mouyane, P.E. Lippens, M. Womes, B. Ducourant, J. Olivier-Fourcade, J.C. Jumas, Hyperfine Interact. 187 (2008) 27–34.
[14] M. Mouyane, J.-M. Ruiz, M. Artus, S. Cassaignon, J.-P. Jolivet, C.J.G. Caillon, K. Driesen, J. Scoyer, L. Stievano, J. Olivier-Fourcade, J.-C. Jumas, J. Power Sources 196 (2011) 6863–6869.
[15] M. Mouyane, L. Aldon, M. Womes, B. Ducourant, J.-C. Jumas, J. Olivier-Fourcade, J. Power Sources 189 (2009) 818–822.
[16] W. Kündig, Nucl. Instrum. Methods 75 (1969) 336–340.
[17] M. Shibuya, K. Endo, H. Sano, Bull. Chem. Soc. Jpn. 51 (1978) 1363–1367.
[18] R.H. Herber, Y. Hazony, Techniques of Chemistry, Wiley, New York, 1972, p. 278ff.
[19] M. Mouyane, M. Womes, J.C. Jumas, J. Olivier-Fourcade, P.E. Lippens, J. Solid State Chem. 184 (2011) 2877–2886.
[20] D. Niemeier, H. Mehner, U. Bismayer, K.D. Becker, Phys. Status Solidi B 211 (1999) 581–594.
[21] D.E. Conte, A. Aboulaich, F. Robert, J. Olivier-Fourcade, J.C. Jumas, C. Jordy, P. Willmann, J. Solid State Chem. 183 (2010) 65–75.
[22] K.F.E. Williams, C.E. Johnson, J.A. Johnson, D. Holland, M.M. Karim, J. Phys.: Condens. Matter 7 (1995) 9485–9497.
[23] V.A. Varnek, L.V. Chernikova, V.I. Kazakova, V.E. Dyakov, Ind. Lab. 56 (1990) 680–683.
[24] P.E. Lippens, L. Aldon, C.M. Ionica, F. Robert, J. Olivier-Fourcade, J.C. Jumas, in: P. Knauth, C. Masquelier, E. Traversa, E.D. Wachsman (Eds.), Solid State Ionics-2004, Materials Research Society Symposium Proceedings, vol. 835, Materials Research Society, Warrendale, 2005, pp. 249–260.
[25] F. Robert, P.E. Lippens, J. Olivier-Fourcade, J.C. Jumas, F. Gillot, M. Morcrette, J.M. Tarascon, J. Solid State Chem. 180 (2007) 339–348.
[26] I.A. Courtney, J.R. Dahn, J. Electrochem. Soc. 144 (1997) 2045–2052.
[27] H. Kim, B. Park, H.J. Sohn, T. Kang, J. Power Sources 90 (2000) 59–63.
[28] K.C.P. Villars, J. Daams, R. Gladyshevskii, O. Shcherban, V. Dubenskyy, V. Kuprysyuk, O. Pavlyuk, I. Savysyuk, S. Stoyko, Group III Condensed Matter, vol. 43A7, Landolt-Börnstein, Springer, Berlin, Heidelberg, 2009, ISBN 978-3-540-69948-4.
[29] A. Aboulaich, F. Robert, P.E. Lippens, L. Aldon, J. Olivier-Fourcade, P. Willmann, J.C. Jumas, Hyperfine Interact. 167 (2006) 733–738.
[30] J. Chouvin, C.P. Vicente, J. Olivier-Fourcade, J.C. Jumas, B. Simon, P. Biensan, Solid State Sci. 6 (2004) 39–46.
[31] P.E. Lippens, Phys. Rev. B 605 (1999) 4576–4586.